


Article

# Process and High-Temperature Oxidation Resistance of Pack-Aluminized Layers on Cast Iron

Xing Wang , Yongzhe Fan, Xue Zhao, An Du \*, Ruina Ma \* and Xiaoming Cao

Key Lab for New Type of Functional Materials in Hebei Province, Tianjin Key Lab Material Laminating Fabrication and Interface, School of Material Science and Engineering, Hebei University of Technology, Tianjin 300132, China; wangxinggr@163.com (X.W.); fyz@hebut.edu.cn (Y.F.); zhaoxue@hebut.edu.cn (X.Z.); caoxiaoming@hebut.edu.cn (X.C.)

\* Correspondence: duan@hebut.edu.cn (A.D.); maryna@126.com (R.M.);  
Tel.: +86-159-0226-6022 (A.D.); +86-136-4207-4657 (R.M.)

Received: 15 May 2019; Accepted: 1 June 2019; Published: 4 June 2019



**Abstract:** Pack aluminizing of spheroidal graphite cast iron with different aluminizing temperature and time was studied. Results showed that the thickness of aluminized layer increased with the increasing temperature and time. The optimized process parameters are as follow: the aluminizing packed temperature is 830 °C and the time is 3 h. The aluminized layer consisted of the inner FeAl and the outer Fe<sub>2</sub>Al<sub>5</sub>. Some graphite nodules were observed in the aluminide layer after aluminizing. The mass gain of the aluminized cast iron was 0.405 mg/cm<sup>2</sup>, being 1/12 of the untreated substrate after oxidation. The high temperature oxidation resistance can be improved effectively by pack aluminizing, even though there were graphite nodules in the aluminide layer.

**Keywords:** spheroidal graphite cast iron; pack aluminizing; microstructure; high-temperature oxidation resistance

## 1. Introduction

Spheroidal graphite cast irons have good thermal conductivity, excellent fatigue resistance and high strength. Therefore, components such as engine parts, brake pads and heat exchangers with the requests of high temperature and excellent fatigue resistance are made of cast irons [1,2]. In recent years, the maximum combustion temperature increased with the raising of car speed, resulting in the use of coatings to protect spheroidal graphite cast iron [3].

Previous researches have shown that FeAl intermetallic phases such as Fe<sub>2</sub>Al<sub>5</sub>, FeAl<sub>3</sub>, and FeAl could effectively increase the high-temperature oxidation resistance [4–6]. This is because intermetallic phases such as Fe<sub>2</sub>Al<sub>5</sub>, FeAl<sub>3</sub>, and FeAl can protect the metal surface by continuously forming Al<sub>2</sub>O<sub>3</sub> film. Plasma spraying [7], slurry aluminizing [8], hot dipping and pack aluminizing [9,10] are the major technologies to form FeAl coatings. Packing aluminizing is a method that the workpiece and the powder aluminizing agent are loaded into a sealed aluminizing box, and then the surface is aluminized by heating, heat preservation, and diffusion annealing. Among these methods, pack aluminizing offers the advantage of forming coating over different shapes and sizes of components, such as engine parts [11].

The majority of reports of pack aluminizing were about carbon steel, stainless steel and alloys [12–14]. Above studies have shown that pack aluminizing could be successfully applied to carbon steel, stainless steel and alloys at low temperature. However, it was under the help of other surface process, such as magnetron sputtering, deep rolling process and plasma nitriding [13,15–17]. Without these treatments, the aluminizing layer obtained at low temperature was very thin with one phase [18]. Thick aluminizing layer and more phases can be obtained at high temperature, but pores

appeared in the FeAl layers [19]. For Ni-based alloys and Ti-based alloys, the aluminizing temperature should be higher than 1050 °C and 1000 °C respectively to form the pack aluminizing coatings [20,21].

Cast irons are consisted of a large number of C and Si elements which hinder the Al diffusion. In addition, spheroidal graphites located in substrate are obstacle [21]. Many efforts have been made on hot dip aluminizing to produce iron aluminum intermetallic layer on cast iron [6,22]. However, the adhesion of alumina scale over the aluminide coating has been a major concern. The coating formed by pack aluminizing has good adhesion. Currently, there is no information available concerning pack aluminizing on spheroidal graphite cast irons. As a result, basic researches on pack aluminizing technology were conducted in our study.

This paper reported the effects of aluminizing temperature and time on the microstructure and thickness of aluminide layer during pack aluminizing on spheroidal graphite cast irons. Moreover, the high temperature oxidation resistance was also evaluated.

## 2. Experiment

Spheroidal graphite cast irons (QT420, Ningbo Zhongbo metal material Co. Ltd., 4 grade, fully ferritic, Zhejiang, China) were employed as substrate material. The chemical composition provided by supplier of the cast iron is shown in Table 1. The dimension of the specimens approximately 10 mm × 10 mm × 4 mm. The specimens were ground by using silicon carbide waterproof abrasive paper to a 1200-grade finish and ultrasonically cleaned in ethanol. The pack powder mixture was consisted of 25Al-2NH<sub>4</sub>Cl-73Al<sub>2</sub>O<sub>3</sub> (wt. %). The samples were placed in cylinders which were sealed with quartz grains and refractory clay. The sealed cylinders were placed inside a box-type furnace and pack aluminized at the temperature range from 800 °C to 880 °C for 1 h to 5 h.

**Table 1.** Composition of the cast iron (wt %).

C	Si	Mn	P	S	Fe
3.0	1.6	0.7	0.5	0.12	allowance

The packing aluminized samples were polished. The cross-sectional microstructure of aluminide layer was observed by a Hitachi S-4800 microscope (SEM, Suzhou Seins Instrument Co. Ltd., Suzhou, China). The average value of aluminized coating thickness was obtained from 6 lengths, which include the maximum and the minimum. The XRD test of the permeable layer cross section adopts the method of layer by layer separation: using silicon carbide sandpaper to polish the permeable layer, and determine the grinding thickness through the metallographic microscope. X-ray diffractometer (XRD, Brook AXS Co. Ltd., Los Angeles, CA, USA) was used to determine the phase composition of the infiltration layer and the oxide layer. CuK<sub>α</sub> was adopted, and the sweeping speed was 4 °/min. The test Angle was: the infiltration layer was 20–83°, and the oxidation layer was 10–90°. The phases of the aluminide layer were identified with a D8-Discover X-ray Diffraction.

The aluminized samples were polished with 400# sandpaper until the surface appears bright white to remove the oxide scale on the surface. Then they were put into a ceramic crucible, and then heated by a box-type furnace. High temperature oxidation experiments were carried out at 750 °C in static air for 72 h to estimate high temperature oxidation resistance. The masses of specimens were measured with a precision electronic balance (0.1 mg accuracy) after oxidation experiments.

## 3. Results and Discussion

### 3.1. Effect of Pack Aluminizing Time on the Aluminide Layers

The cross-sectional microstructures of the aluminizing samples with different pack aluminizing times are shown in Figure 1. It can be noticed that the spheroidal graphites are observed in the aluminide layer where the coating is not formed successfully as shown in Figure 1a–e. The irregular coatings result from the spheroidal graphites in the coatings which inhibit the diffusion of Al and Fe.

In addition, the growth direction of the pack aluminide layers formed inside the matrix is confirmed. Because the diffusion rate of Al atoms is faster than that of Fe atoms [23], the spheroidal graphites are trapped gradually in the aluminide layers.

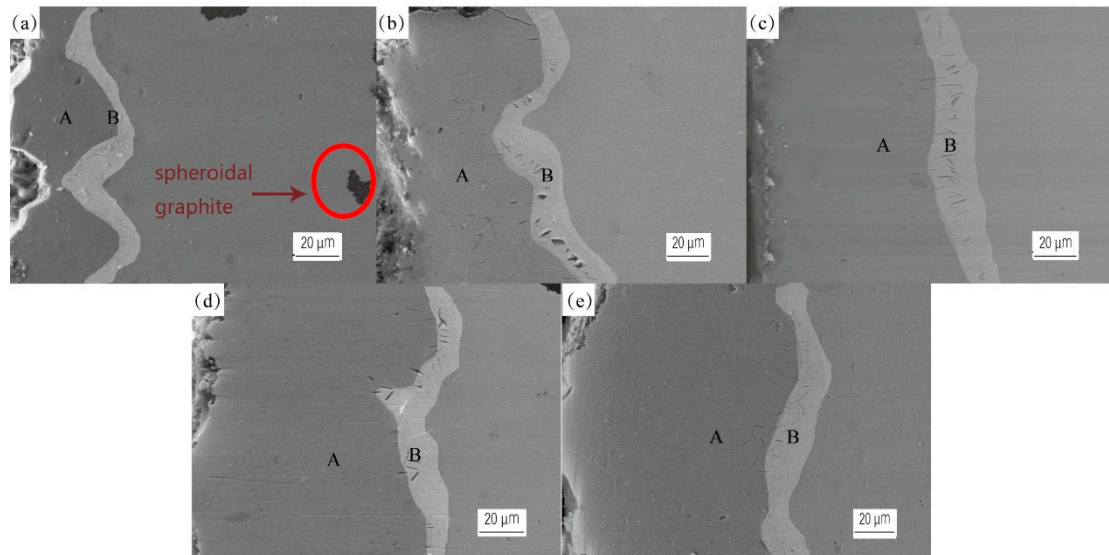


**Figure 1.** The cross-sectional microstructures of aluminizing samples at 830 °C (a) for 1 h; (b) for 2 h; (c) for 3 h; (d) for 4 h; (e) for 5 h.

There are two distinct regions in aluminized coating which include the outer layer A and the inner layer B. The layer A obtained at different time is dense and with no pores while some needles can be observed in the layer B, and the growth direction of needles are perpendicular to the aluminide layer (Figure 1a–e). The appearance of the needle can be explained from two aspects: on the one hand, because of the presence of dense oxide film, only Al atom migrated outward during the oxidation process. When Al atom enters the oxide film from the metal/oxide film section, it will leave a vacancy in the metal lattice, and the vacancy migrates inward to the metal/oxide film section in the opposite direction, and the vacancy diffuses to the appropriate position and precipitates to form needle-like holes. On the other hand, the difference of Fe and Al concentration between the high-temperature infiltration layer and the matrix finally leads to the formation of the needle [3]. The gamma region is strongly shrunk because of the infiltration of Al atoms. Recrystallization of gamma-alpha ( $\text{Al}_2\text{O}_3$ ) occurs after austenite saturation [24,25]. After aluminizing for 1 h, the interface between the aluminide layer and substrate is fairly irregular owing to the preferential and fast aluminide layer growth in the early stage of aluminizing (Figure 1a). In addition, the diffusion depth of Al atoms is relatively small, so the aluminide layer is very thin. With prolonging the aluminizing time, the interface of aluminide layer and substrate becomes smooth. Besides, the thickness of the layer also increases owing to the further diffusion of the active Al, as shown in Figure 2. About 95  $\mu\text{m}$  thick aluminide layer is produced on cast iron at 3 h. Aluminate coating was prepared through the method of slurry aluminizing with a activator of  $\text{AlCl}_3$ , of which the thickness is only about 60  $\mu\text{m}$  [26]. And the interface between the intermetallic layer and cast iron is smooth and regular (Figure 1d). The aluminide layer thickness increases rapidly in the first 3 h then slows down afterward, The Al atoms are not integrated into the matrix lattice, because the solid solubility of Al atoms in Fe based solid solution reaches the limit with the long diffusion time. Thus, the longer aluminizing time has no obvious influence on the aluminizing layer thickness. In addition, the edges of samples will rise with the prolonging aluminizing time owing to bond of pack powder mixture [18].

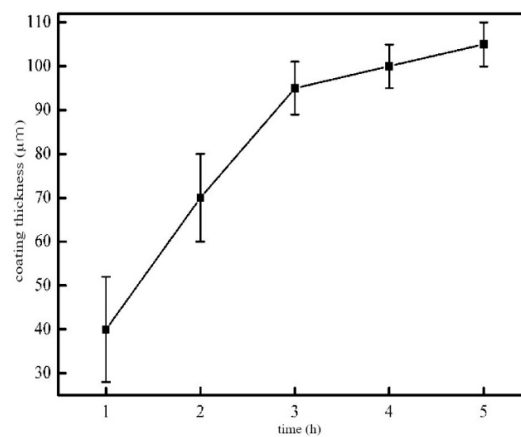


**Figure 2.** Aluminide layer thickness changing with aluminizing time.

### 3.2. Effect of Aluminizing Temperature on the Aluminizing Layer

Figure 3 shows the cross section micrograph of the sample with the aluminizing time of 3 h at four different temperatures and Figure 4 illustrates the relationship between the aluminide layer thickness and temperature. The relationship is the same as the Fick's law of diffusion which describes that the thickness of the diffusion layers increases with elevated temperature [27]. The low kinetic energy of the active Al results in the slow diffusion rate at 800 °C. With the rise of aluminizing temperature, the diffusion rate increases, so the thickness of the aluminide layer increases. However, the aluminide layer thickness increases slowly when the aluminide layer is up to a suitable thickness. It can be seen from Figure 3 that only 20 μm thick aluminide layer is produced on cast iron at 800 °C. With the increase of aluminizing temperature, the aluminide layer thickness increases quickly, which is 140 μm at 880 °C. However, the interface between the aluminide layer and the cast iron is irregular (Figure 3d), and the edges of samples rise because of the accumulation of the active Al.

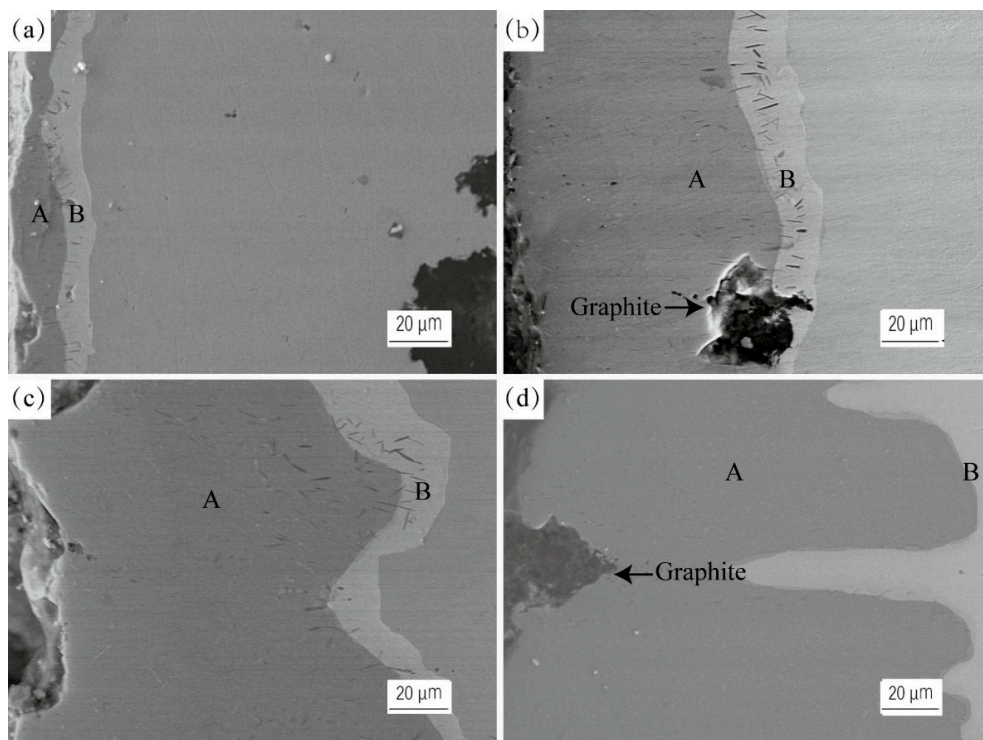


**Figure 3.** The cross-sectional microstructures of aluminizing samples at (a) 800 °C; (b) 830 °C; (c) 850 °C; (d) 880 °C.

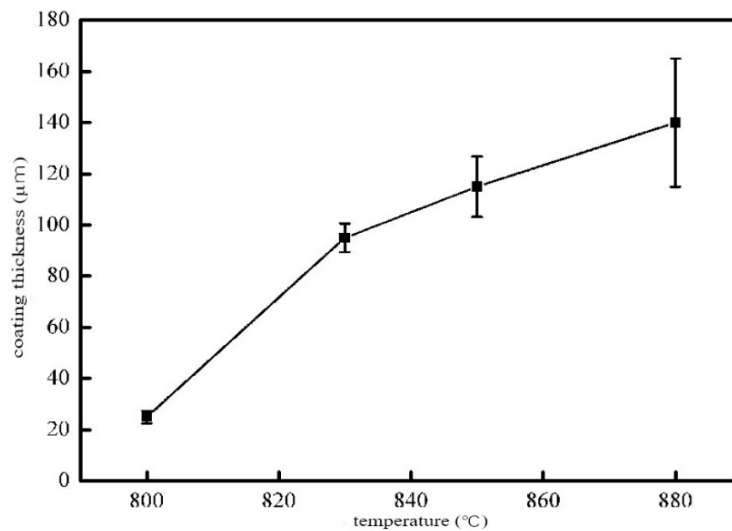


**Figure 4.** Aluminide layer thickness changing with aluminizing temperature.

### 3.3. Microstructure of Aluminizing Layer

Above all, in order to obtain a better quality coating, the technological parameters of packing aluminizing adopted in this report are packed at 830 °C for 3 h. The aluminide layer thickness is about 95 μm with the adopted optimized process.

Figure 5 shows the energy-dispersive spectrometry (EDS) test location of the aluminized layer. Figure 5a shows the surface of the aluminized layer, and Figure 5b shows the section of the aluminized layer. In Figure 5a point I was selected on the permeability layer surface. Point II represents the permeability layer between the outer area and the inner layer, point III is located in the outer and inner regions near the permeability layer, point IV carbonitriding layer between the inner, V in matrix and close to the carbonitriding layer inner regions, VI for the inside of a matrix. The analysis results are shown in Table 2. The percentage of Al atoms in the outer layer of the infiltration layer is between 69.55% and 73.88%, while the percentage of Fe atoms is less than 30%. In the inner layer of the permeable layer, the percentage of Al atoms is about 50%, and the percentage of Fe atoms is also 50%. It can be inferred from FeAl binary phase diagram that the outer layer of infiltration layer is  $Fe_2Al_5$  phase and inner layer of the infiltration layer is FeAl phase. In the matrix and near the inner layer of the permeable layer, the content of Al atom is 13.94%, and the content of Fe atom is 86.07%. Therefore, it can be speculated that Al atoms in this region dissolve in Fe atoms to form a solid solution. With the increasing distance to the surface of the permeable layer, the content of Al atom in the matrix decreased to 5%.

**Table 2.** The EDS analysis of aluminide layer under optimal technology.

Region	Al (at. %)	Fe (at. %)
I	73.88	26.22
II	71.89	28.11
III	69.55	30.45
IV	49.63	50.37
V	13.93	86.07
VI	05.21	94.79

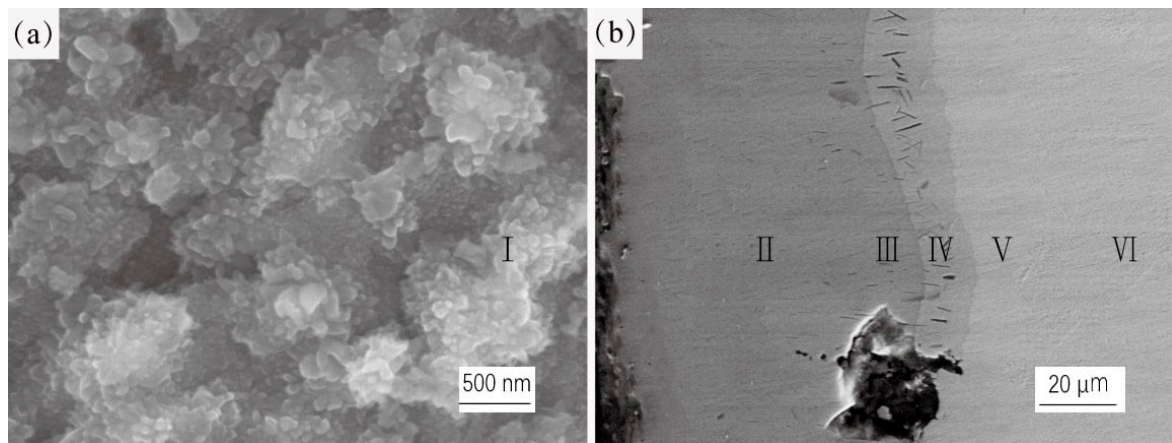


**Figure 5.** The test region of energy-dispersive spectrometry (EDS) under optimal technology (a) the surface of aluminide layer; (b) the cross-sectional of aluminide layer.

Figure 6 are the X-ray diffraction patterns of pack aluminizing cast iron at 830 °C for 3 h. Combined with EDS, the Figure 6 revealed that the layer A is  $\text{Fe}_2\text{Al}_5$  (PDF#47-1435) and the layer B is FeAl (PDF#33-0020) (Figures 1 and 3). Therefore, the intermetallic layer consists of the outer  $\text{Fe}_2\text{Al}_5$  and the inner FeAl.

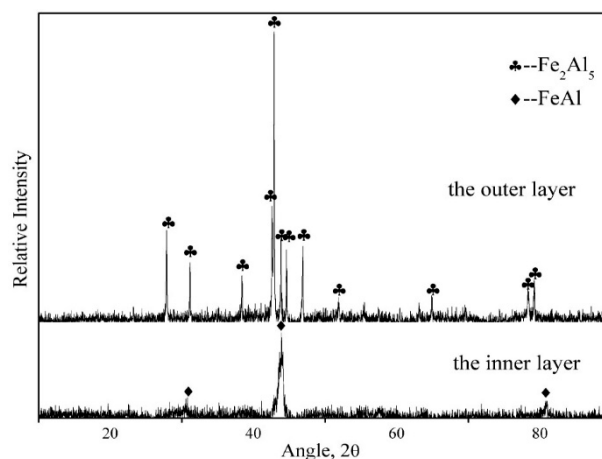


**Figure 6.** X-ray diffraction patterns of pack aluminizing spheroidal graphite cast iron.

### 3.4. High-Temperature Oxidation Kinetics

Samples (830 °C/3 h) were selected for oxidation experiments. Figure 7 shows the mass gain curves of substrate and the aluminide layer oxidized in static air at 750 °C. It is obvious that the weight gain of the aluminizing cast iron is less than that of substrate after oxidation at 750 °C for 72 h. When the oxidation time is up to 72 h, the mass gain of the coated cast iron is 0.435 mg/cm<sup>2</sup>. The high-temperature oxidation test indicated that the aluminide layer could protect the substrate from oxidation permeating effectively. In addition, when the oxidation time reaches 72 h, the mass gain of the coating exceeded 2.0 mg/cm<sup>2</sup> by packing aluminizing on Ti-45Al-8Nb-0.5 (B, C) alloy [21]. The comparison of mass gain indicates that the aluminide layer after pack aluminizing has better high-temperature oxidation resistance than the hot-dipping layer. Using hot dip plating method in Ti-6Al-4V alloy aluminum plating, the coating weight increase is 0.582 mg·cm<sup>-1/2</sup>·h<sup>-1/2</sup> [28].

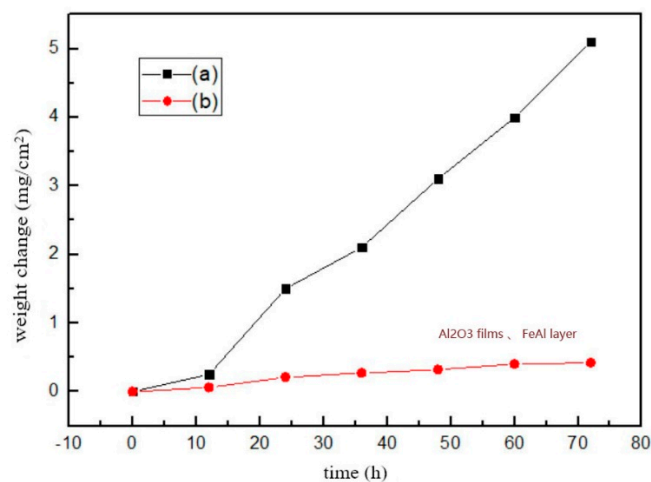


**Figure 7.** Oxidation kinetics at 750 °C in air (a) spheroidal graphite cast iron (b) pack aluminizing.

### 3.5. Microstructures and Phases of Oxidized Specimens

#### 3.5.1. Cast Iron Substrate in Original Condition

It can be seen that the oxide layer consists of two parts and the aggregate thickness of oxide layer is 180  $\mu\text{m}$ . The X-ray diffraction and EDS analysis proved that the oxide layer consists of the outside  $\text{Fe}_3\text{O}_4$  (PDF#26-1136) and the inside  $\text{Fe}_2\text{O}_3$  (PDF#54-0489) (Figure 8a). Visual inspections of bare substrate oxidized at 750 °C for 72 h indicated that the appearance of samples is blank and loose. The cross-sectional micrograph of cast iron is plotted in Figure 9a. Furthermore, the majority of spheroidal graphites included in oxide layer are oxidized as shown in Figure 9a. The oxidation of spherical graphite is attributed to the continuous infiltration of O atoms to form carbides [29]. In this study, the weight gain curve of bare substrate raises slowly in the first 12 h of oxidation. The reason is that the weight reduction caused by decarbonization is less than weight gains caused by oxygen entering.

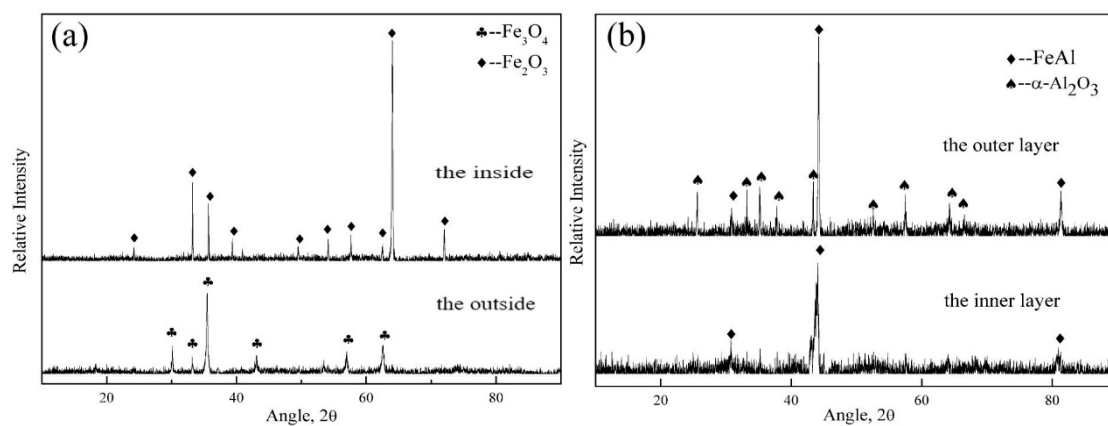


**Figure 8.** X-ray diffraction patterns of substrate oxidized at 750 °C for 72 h (a) spheroidal graphite cast iron (b) pack aluminizing.

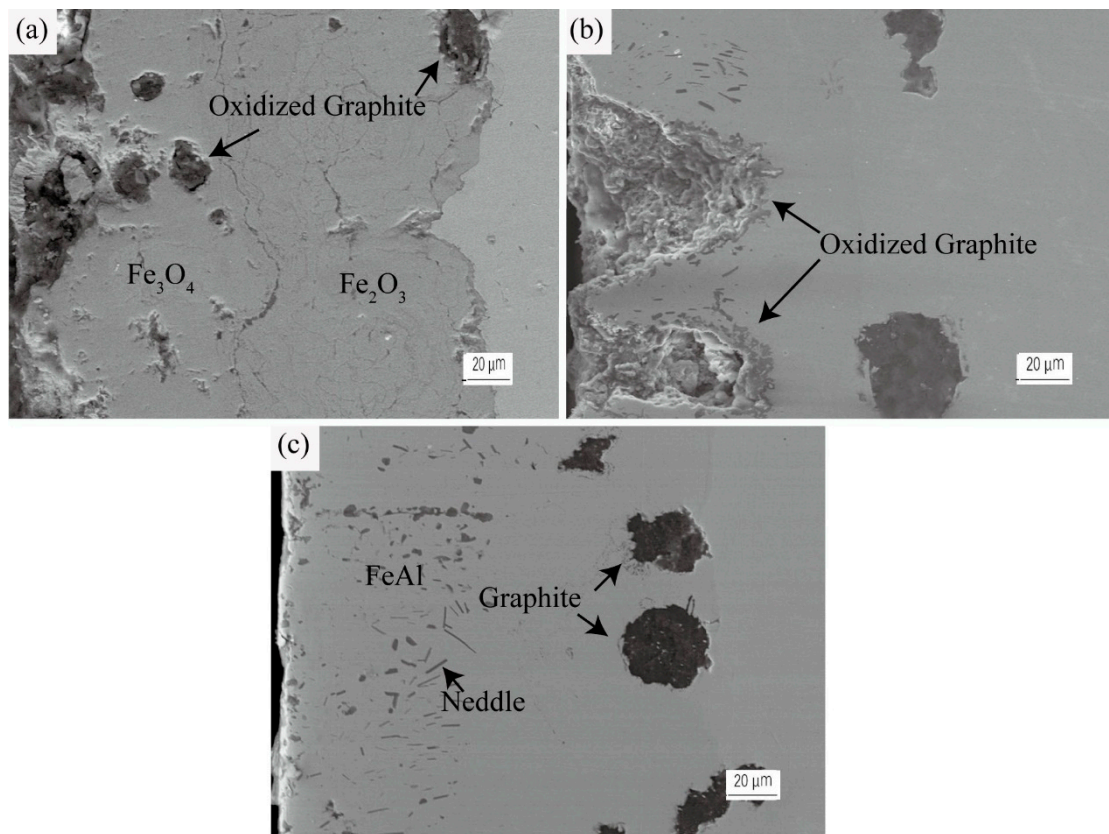


**Figure 9.** The cross-sectional micrographs of samples after the 750 °C oxidation for 72 h (a) spheroidal graphite cast iron (b) and (c) spheroidal graphite cast iron after pack aluminizing.

### 3.5.2. Cast Iron after Pack Aluminizing

Visual inspections of aluminide cast iron oxidized at 750 °C for 72 h indicated that the appearance of samples is gray and has a metallic luster on the surface. Figure 9b,c shows the cross-sectional micrograph of aluminide cast iron after oxidation at 750 °C for 72 h. It can be seen that spheroidal graphites contained in aluminide layer are also oxidized. Oxygen penetrated along the cracks and pores in the aluminide layer left caused by oxidized spheroidal graphites. However, the spheroidal graphites in substrate are not oxidized. In addition, there is only one FeAl layer after oxidation and there are many needles in FeAl layer. During high temperature oxidation, the FeAl layer begins to expand.

Figure 8b shows the phases of aluminide coating on cast iron after high temperature oxidation at 750 °C for 72 h. It shows that the aluminide layer consists of  $Al_2O_3$  films and FeAl layer after oxidation. The  $Fe_2Al_5$  which formed in the pack aluminizing process, was not found [26]. The reason of disappearance of  $Fe_2Al_5$  are that the inward diffusion of Al from aluminide layer and the outward diffusion of Fe. Therefore, the  $Fe_2Al_5$  and transforms to FeAl phase. In the early stage of oxidation,  $Al_2O_3$  films which form on the surface of aluminide layer can prevent the oxidation from permeating the substrate effectively. Combining with Figure 7b, the reason for the slow growth of weight gain curve of aluminized substrate in early oxidation is the joint effect of decarbonization and oxygen permeating.

In this study, the pores and cracks produced by oxidized spheroidal graphites lead to oxidation of the certain region of substrate. However, the aluminide layer still plays a role. The high temperature tests indicated that the weight gain of the aluminizing specimens is less than that of substrate after oxidation at 750 °C for 72 h. The coating obtained by pack aluminizing can protect the substrate form oxidation permeating effectively at 750 °C.



#### 4. Conclusions

Spheroidal graphite cast irons were aluminized by pack aluminizing. The thickness of the aluminide layer increased with increasing aluminizing time up to 4 h, after that, it increased very slowly with increasing time. The rise of temperature also caused the increase of thickness. However, if the temperature exceeded 880 °C, the interface between the aluminide layer and the cast iron was irregular. Furthermore, the protrude edges of sample resulted from accumulation of active Al. The phases of aluminide layer were made up the inner FeAl and outer Fe<sub>2</sub>Al<sub>5</sub>.

The spheroidal graphite in the substrate was observed in the aluminide layer after pack aluminizing. The mass gain of the coated cast iron was 0.435 mg/cm<sup>2</sup>, being 1/12 of spheroidal graphite cast iron after oxidation resulting from the formation of Al<sub>2</sub>O<sub>3</sub> films on the cast iron substrate. The aluminide layer could effectively prevent the substrate from oxidation at 750 °C, even though there was spheroidal graphite in the aluminide layer.

**Author Contributions:** Writing–Original Draft Preparation, X.W.; Conceptualization, Y.F.; Data Curation, X.Z.; Methodology, A.D.; Resources, R.M.; Formal Analysis, X.C.

**Funding:** This research received no external funding.

**Acknowledgments:** This work was supported by (The National Natural Science Foundation of China); Under Grand (number 51501055 and 51601056).

**Conflicts of Interest:** The authors declare no conflict of interest.

#### References

1. Di Cocco, V.; Iacoviello, F.; Rossi, A.; Cavallini, M.; Natali, S. Graphite nodules and fatigue crack propagation micromechanisms in a ferritic ductile cast iron. *Fatigue Fract. Eng. Mater. Struct.* **2013**, *36*, 893–902. [[CrossRef](#)]
2. Li, Y.; Dong, S.; Yan, S.; Liu, X.; He, P.; Xu, B. Surface remanufacturing of ductile cast iron by laser cladding Ni-Cu alloy coatings. *Surf. Coat. Technol.* **2018**, *347*, 20–28. [[CrossRef](#)]
3. Zhang, Y.; Fan, Y.; Zhao, X.; Du, A.; Ma, R.; Wu, J.; Cao, X. Influence of Graphite Morphology on Phase, Microstructure, and Properties of Hot Dipping and Diffusion Aluminizing Coating on Flake/Spheroidal Graphite Cast Iron. *Metals* **2019**, *9*, 450. [[CrossRef](#)]
4. Bates, B.L.; Wang, Y.Q.; Zhang, Y.; Pint, B.A. Formation and oxidation performance of low-temperature pack aluminide coatings on ferritic-martensitic steels. *Surf. Coat. Technol.* **2009**, *204*, 766–770. [[CrossRef](#)]
5. Wang, C.J.; Badaruddin, M. The dependence of high temperature resistance of aluminized steel exposed to water-vapour oxidation. *Surf. Coat. Technol.* **2010**, *205*, 1200–1205. [[CrossRef](#)]
6. Jiang, W.; Fan, Z.; Li, G.; Liu, X.; Liu, F. Effects of hot-dip galvanizing and aluminizing on interfacial microstructures and mechanical properties of aluminum/iron bimetallic composites. *J. Alloys Compd.* **2016**, *688*, 742–751. [[CrossRef](#)]
7. Dhakar, B.; Chatterjee, S.; Sabiruddin, K. Phase stabilization of spraying mechanically blended alumina-chromia powders. *Mater. Manuf. Processes* **2017**, *32*, 355–364. [[CrossRef](#)]
8. Pedraza, F.; Boulesteix, C.; Proy, M.; Lasanta, I.; de Miguel, T.; Illana, A.; Pérez, F.J. Behavior of Slurry Aluminized Austenitic Stainless Steels under Steam at 650 and 700 °C. *Oxid. Met.* **2017**, *87*, 443–454. [[CrossRef](#)]
9. Abro, M.A.; Lee, D.B. High temperature corrosion of hot-dip aluminized steel in Ar/1% SO<sub>2</sub> gas. *Met. Mater. Int.* **2017**, *23*, 92–97. [[CrossRef](#)]
10. Wu, L.-K.; Wu, J.-J.; Wu, W.-Y.; Hou, G.-Y.; Cao, H.-Z.; Tang, Y.-P.; Zhang, H.-B.; Zheng, G.-Q. High temperature oxidation resistance of gamma-TiAl alloy with pack aluminizing and electrodeposited SiO<sub>2</sub> composite coating. *Corros. Sci.* **2019**, *146*, 18–27. [[CrossRef](#)]
11. Kochmanska, A.E. Microstructure of Al-Si Slurry Coatings on Austenitic High-Temperature Creep Resisting Cast Steel. *Adv. Mater. Sci. Eng.* **2018**, *2018*, 5473079. [[CrossRef](#)]
12. Huang, M.; Wang, Y.; Zhang, M.-X.; Huo, Y.-Q.; Gao, P.-J. Effect of magnetron-sputtered Al film on low-temperature pack-aluminizing coating for oil casing steel N80. *Surf. Rev. Lett.* **2014**, *21*, 1450053. [[CrossRef](#)]

13. Yutanorm, W.; Juijerm, P. Diffusion enhancement of low-temperature pack aluminizing on austenitic stainless steel AISI 304 by deep rolling process. *Kovove Mater.* **2016**, *54*, 227–232. [[CrossRef](#)]
14. Ma, F.; Gao, Y.; Zeng, Z.; Liu, E. Improving the Tribocorrosion Resistance of Monel 400 Alloy by Aluminizing Surface Modification. *J. Mater. Eng. Perform.* **2018**, *27*, 3439–3448. [[CrossRef](#)]
15. Zhan, Z.; Liu, Z.; Liu, J.; Li, L.; Li, Z.; Liao, P. Microstructure and high-temperature corrosion behaviors of aluminide coatings by low-temperature pack aluminizing process. *Appl. Surf. Sci.* **2010**, *256*, 3874–3879. [[CrossRef](#)]
16. Son, Y.I.; Chung, C.H.; Gowkanapalli, R.R.; Moon, C.H.; Park, J.S. Kinetics of Fe<sub>2</sub>Al<sub>5</sub> phase formation on 4130 steel by Al pack cementation and its oxidation resistance. *Met. Mater. Int.* **2015**, *21*, 1–6. [[CrossRef](#)]
17. Wang, J.; Wu, D.J.; Zhu, C.Y.; Xiang, Z.D. Low temperature pack aluminizing kinetics of nickel electroplated on creep resistant ferritic steel. *Surf. Coat. Technol.* **2013**, *236*, 135–141. [[CrossRef](#)]
18. Majumdar, S.; Paul, B.; Kain, V.; Dey, G.K. Formation of Al<sub>2</sub>O<sub>3</sub>/Fe-Al layers on SS 316 surface by pack aluminizing and heat treatment. *Mater. Chem. Phys.* **2017**, *190*, 31–37. [[CrossRef](#)]
19. Lee, J.-W.; Kuo, Y.-C. A study on the microstructure and cyclic oxidation behavior of the pack aluminized Hastelloy X at 1100 °C. *Surf. Coat. Technol.* **2006**, *201*, 3867–3871. [[CrossRef](#)]
20. Priest, M.S.; Zhang, Y. Synthesis of clean aluminide coatings on Ni-based superalloys via a modified pack cementation process. *Mater. Corros.* **2015**, *66*, 1111–1119. [[CrossRef](#)]
21. Szkliniarz, W.; Moskal, G.; Szkliniarz, A.; Swadzba, R. The Influence of Aluminizing Process on the Surface Condition and Oxidation Resistance of Ti-45Al-8Nb-0.5(B, C) Alloy. *Coatings* **2018**, *8*, 113. [[CrossRef](#)]
22. Lin, M.-B.; Wang, C.-J.; Volinsky, A.A. Isothermal and thermal cycling oxidation of hot-dip aluminide coating on flake/spheroidal graphite cast iron. *Surf. Coat. Technol.* **2015**, *206*, 1595–1599. [[CrossRef](#)]
23. Lin, M.-B.; Wang, C.-J. Microstructure and high temperature oxidation behavior of hot-dip aluminized coating on high silicon cast iron. *Surf. Coat. Technol.* **2010**, *205*, 1220–1224. [[CrossRef](#)]
24. Wang, S.; Zhou, L.; Li, C.; Li, Z.; Li, H. Morphology and Wear Resistance of Composite Coatings Formed on a TA2 Substrate Using Hot-Dip Aluminising and Micro-Arc Oxidation Technologies. *Materials* **2019**, *12*, 799. [[CrossRef](#)] [[PubMed](#)]
25. Boulesteix, C.; Pedraza, F. Suitable sealants for cracked aluminized austenitic steels and their oxidation behavior. *Surf. Coat. Technol.* **2017**, *327*, 9–17. [[CrossRef](#)]
26. Sun, Y.; Dong, J.; Zhao, P.; Dou, B. Formation and phase transformation of aluminide coating prepared by low-temperature aluminizing process. *Surf. Coat. Technol.* **2017**, *330*, 234–240. [[CrossRef](#)]
27. Cheng, W.-J.; Wang, C.-J. Growth of intermetallic layer in the aluminide mild steel during hot-dipping. *Surf. Coat. Technol.* **2009**, *204*, 824–828. [[CrossRef](#)]
28. Jeng, S.-C. Oxidation behavior and microstructural evolution of hot-dipped aluminum coating on Ti-6Al-4V alloy at 800 °C. *Surf. Coat. Technol.* **2013**, *235*, 867–874. [[CrossRef](#)]
29. Tholence, F.; Norell, M. Nitride precipitation during high temperature of ductile cast irons in synthetic exhaust gases. *J. Phys. Chem.* **2005**, *66*, 530–534. [[CrossRef](#)]

